SANDIA REPORT

SAND97-8240 • UC-404
Unlimited Release
Printed February 1997

A Locally Analytic Density Functional Theory Describing Adsorption and Condensation in Microporous Materials

R. H. Nilson, S. K. Griffiths

Prepared by
Sandia National Laboratories
Albuquerque, New Mexico 87185 and Livermore, California 94550
for the United States Department of Energy
under Contract DE-ACO4-94AL85000

Issued by Sandia National Laboratories, operated for the United States Department of Energy by Sandia Corporation.

Available to DOE and DOE contractors from:

Office of Scientific and Technical Information
P.O. Box 62
Oak Ridge TN 37831

Prices available from (615) 576-8401, FTS 626-8401.

Available to the public from:

National Technical Information Service
U.S. Department of Commerce
5285 Port Royal Rd.
Springfield, VA 22161

UC-404

SAND97-8240
Unlimited Release
Printed February 1997

A Locally Analytic Density Functional Theory Describing Adsorption and Condensation in Microporous Materials

Robert H. Nilson and Stewart K. Griffiths
Sandia National Laboratories
Livermore, California 94551-0969

The fluid density distribution within microscopic pores is determined by solving integral equations relating the local chemical potential to the van der Waals attractions and hard sphere repulsions of surrounding material. To avoid resolving the density distribution on sub-molecular scales, the governing equations are averaged over zones of molecular size using analytic functions to represent local density variations within each zone. These local density profiles range from singularities to uniform distributions depending on the local variation of the potential field. Sample calculations indicate that this integral approach yields results in very good agreement with those based on traditional density functional theory (DFT), while reducing computing times by factors of 10^3 to 10^4 for one-dimensional geometries.

Introduction

Intermolecular forces attract gas molecules to solid surfaces. Because this attraction to solids is much stronger that the mutual attraction between gas molecules, gases tend to form a thin high-density layer adjacent to any solid surface. Such layers may reach liquid-like densities even at pressures orders-of-magnitude below that at which bulk condensation would normally occur. The thickness of these liquid-like adsorbed layers grows with increasing pressure, but rarely exceeds a few molecular diameters until the normal condensation pressure is reached [1,2].

The adsorption of gases on solid surfaces is important in several practical applications of porous materials. Silica desiccants and charcoal filters, as well as more sophisticated devices used in the filtration and separation of gases [1], all depend on large specific surface areas to attract and store large quantities of gases in a relatively small physical volume. In some applications, the performance of these materials can be enhanced by reducing pore sizes to near-molecular dimensions. In such small pores, gases are attracted by the overlapping potential fields of opposing pore walls. The increased attraction promotes adsorption and reduces the pressure at which gas in the center of the pore condenses to form a liquid. This marked reduction in condensation pressure permits the low pressure storage of gases at mean densities near liquid values.

Another common application of this adsorption phenomenon is in characterizing the microstructure of porous materials. Here, a measured adsorption isotherm, depicting the amount of gas adsorbed as a function of the external pressure [2], is used to deduce the surface area and sometimes the pore size distribution. For materials having relatively large pores, the measured isotherm of a material sample is compared with a theoretical isotherm for a flat surface to obtain an estimate of the surface area. For materials having molecular-scale pores, both the surface area and pore size distribution must be estimated together. In this case, a candidate pore size distribution is varied to obtain the best agreement between the measured isotherm and a composite isotherm that includes contributions from all candidate pores sizes,

weighted by their respective surface areas [3,4,5,6]. This method requires theoretical predictions of the complete isotherm, including condensation, for each pore size in all candidate distributions.

Theoretical predictions of adsorption and condensation are traditionally based on analytical models. The most familiar of these are the Langmuir equation for the pressure-dependent fractional surface coverage of the first adsorbed layer and the BET formula describing the sequential formation of multiple adsorbed layers [7]. Quite distinct from these analyses of adsorption on flat external surfaces, there are two well-known formulas relating condensation pressure to pore size. The classical Kelvin equation applies in the limit of very large pores, whereas the Horvath-Kawazoe model applies in the opposite extreme [8]. Although these analytical models provide many useful insights, a more general approach is needed to predict both adsorption and condensation in all pore sizes.

Numerical models of adsorption and condensation may be separated into three general categories. All three use pair potentials to describe interactions between molecules. In molecular dynamic (MD) simulations the calculated forces between discrete molecules are used to evolve their individual time-dependent trajectories [9]. Monte Carlo (MC) methods replace the lengthy process of time integration with trial-and-error minimization of the free energy followed by ensemble averaging [10]. In contrast to these discrete simulation methods, the mean field approach referred to as density functional theory (DFT) uses a continuum methodology to determine directly the time-averaged density field [9-15]. In this technique, interactions among molecules are represented by density-weighted integrals of the pair potential functions. Although DFT accurately reproduces the results of MD and MC simulations with greatly reduced effort [9-15], computing times for DFT are still measured in hours or even days.

All of these numerical models yield structured density profiles like that shown in Figure 1. The density peaks adjacent to the pore walls reach magnitudes about ten times greater than the bulk liquid density. This is because the molecules in these layers have their centers confined within a very narrow zone coincident with the minimum of the attractive wall potential. Thus the large magnitude and slenderness of the first few peaks reflect the high areal density and planar ordering of the surface atoms of the adjacent solid [16]. With increasing distance from the wall, the fluid becomes less ordered and the peaks rapidly diminish.

Although the occurrence and magnitude of these density peaks are of some theoretical interest, numerical resolution of these features requires a substantial computing effort. This effort can be greatly reduced if the primary purpose of the analysis is to predict the total mass of adsorbed gas. This total adsorption is the only information required for the analysis of the engineering applications noted earlier, including the construction of adsorption isotherms used to infer the pore size distribution of a material.

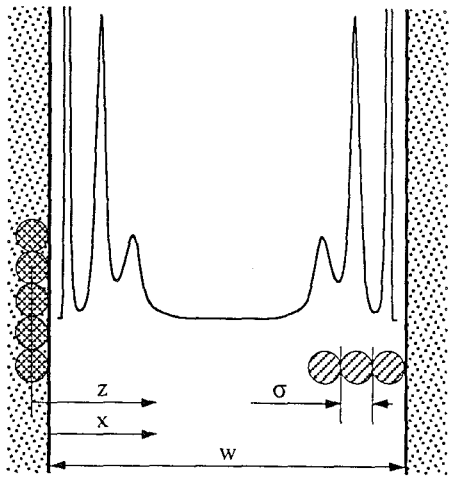

Figure 1. Schematic of adsorption on the walls of a slit pore. Density peaks of the first layers result from localization of molecular centers in the potential well of adjacent solid material. Successive layers are progressively less ordered and have less prominent peaks. Layer spacing is about one molecular diameter.

With this purpose in mind, the present paper describes a locally analytic density functional theory (LADFT) derived by averaging the governing equations over regions of molecular size. In contrast to previous formulations, we make no attempt to resolve sub-molecular details of the density profile by numerical means. Rather, local densities within each computational zone are approximated by analytical profiles. As we will see, this approximation yields results nearly identical to those obtained using traditional DFT methods, but with a very dramatic reduction in required computing times.

Governing Equations

The fluid density distribution in a region of uniform temperature, T, and chemical potential, μ_∞, may be determined by minimizing the grand potential energy functional, Ω [9-15].

$$\Omega[\rho(\mathbf{r})] = \int \Big(f[\rho(\mathbf{r})] + \rho(\mathbf{r})[V(\mathbf{r}) - \mu_\infty] \Big) d\mathbf{r} \quad (1)$$

Here, V is the external potential induced by surrounding solid material, and f is the Helmholtz free energy per unit volume of the fluid. The free energy is composed of an ideal gas component, a mean field attraction, U, and an excess hard sphere repulsion, $\Delta\psi$.

$$f = \rho(\mathbf{r})\Big[kT\big(\ln\left[\Lambda^3\rho(\mathbf{r})\right]-1\big)+\frac{1}{2}U(\mathbf{r})+\Delta\psi(\mathbf{r})\Big] \quad (2)$$

The logarithmic ideal gas component depends on the temperature and the local density, ρ, measured in molecular masses per unit volume, as well as Boltzman's constant, k, and the de Broglie wave length, Λ.

The fluid attraction, U, is defined by a density weighted integral of the pair potential function, u, over the surrounding region.

$$U(\mathbf{r}) = \int \rho(\mathbf{r}')\,u(|\mathbf{r}-\mathbf{r}'|)\,d\mathbf{r}' \quad (3)$$

Although the Lennard-Jones 6-12 potential is utilized in nearly all numerical studies, authors differ in how they extract the attractive part. We follow one common approach by splitting the potential at its crossover point, $r=\sigma$, and cutting it off beyond $r=r_{\max}$.

$$u(r) = 4\,\epsilon_{ff}\left[\left(\frac{\sigma}{r}\right)^{12}-\left(\frac{\sigma}{r}\right)^{6}\right], \quad \sigma < r < r_{\max} \quad (4)$$

Outside this interval, $u=0$. To avoid a slight discontinuity at $r=r_{\max}$, this truncated function is then shifted by subtracting $u(r_{\max})$. This approach provides better agreement with measured isotherms [6] than the alternative procedure of splitting the potential at its minimum [5]. The molecular diameter, σ, and depth of the potential well, ϵ_{ff}, appearing in equation (4) are known approximately for common gases.

The excess fluid repulsion, $\Delta\psi$, is generally derived from an equation of state. Tarazona's formulation [12] based on the Carnahan-Starling equation is widely used because it is simple and agrees well with MC simulations [6,9-15].

$$\Delta\psi(\widehat{\rho}) = kT\,\eta\,\frac{(4-3\eta)}{(1-\eta)^2} \quad \text{where} \quad \eta = \widehat{\rho}\,\frac{\pi d^3}{6} \quad (5)$$

The normalized density, η, represents the volume fraction occupied by molecules having a hard sphere diameter, d, taken here as the Lennard-Jones diameter, σ. In the local density approximation (LDA), the normalized density is based on the local density, that is $\widehat{\rho}(\mathbf{r}) = \rho(\mathbf{r})$, while a smoothed density approximation (SDA) uses a weighted average of the surrounding density field. In the latter case,

$$\widehat{\rho}(\mathbf{r}) = \int \rho(\mathbf{r}')\,\omega(|\mathbf{r}-\mathbf{r}'|)\,d\mathbf{r}' \quad (6)$$

Linear weighting over a sphere of radius σ seems to provide the best overall agreement with measured isotherms and with the results of MC simulations [6,15].

$$\omega(r) = \frac{3}{\pi\sigma^3}\left(1-\frac{r}{\sigma}\right) \quad (7)$$

The use of a mean rather than local density permits the formation of narrow density peaks, consistent with physical expectations and the results of MC simulations.

The fluid-solid interaction potential, V, is obtained by integrating the complete Lennard-Jones pair potential over the solid walls that bound the fluid. The solid density is usually assumed uniform over planar sheets of atoms spaced Δ apart, as in Steel's widely used formula [17].

$$v(z) = \epsilon_w\left[\frac{2}{5}\left(\frac{\sigma_{sf}}{z}\right)^{10}-\left(\frac{\sigma_{sf}}{z}\right)^{4}-\frac{\sigma_{sf}^4}{3\Delta(z+0.61\Delta)^3}\right] \quad (8)$$

Here, z is the distance from the center plane of the surface layer of the solid atoms, σ_{sf} is the effective fluid-solid intermolecular diameter, and ϵ_w contains both the Lennard-Jones well depth, ϵ_{sf}, and the solid density, ρ_s.

$$\epsilon_w = 2\pi\rho_s\epsilon_{sf}\sigma_{sf}^2\Delta \quad (9)$$

In a narrow slit bounded by two walls the external potential is then

$$V(x) = v\left(x+\frac{\sigma_{sf}}{2}\right)+v\left(w-x+\frac{\sigma_{sf}}{2}\right) \quad (10)$$

where the position, x, and the pore width, w, are both measured from the surface of the first layer of atoms in the solid. This is as shown in Figure 1.

Using the definitions above, the grand potential energy functional, Ω, can now be minimized by taking the variation of equation (1) with respect to $\rho(\mathbf{r})$ and equating the result to zero. The resulting Euler-Lagrange equation may be written as

$$kT\ln(\Lambda^3\rho)+U+\Delta\psi(\widehat{\rho})+\widehat{\Delta\psi}'+V=\mu_\infty \quad (11)$$

where

$$\widehat{\Delta\psi}'(\mathbf{r}) = \int \rho(\mathbf{r}')\,\omega(|\mathbf{r}-\mathbf{r}'|)\,\Delta\psi'(\widehat{\rho}(\mathbf{r}'))\,d\mathbf{r}' \quad (12)$$

and

$$\Delta\psi'(\widehat{\rho}) = \frac{d}{d\widehat{\rho}}\left[\Delta\psi(\widehat{\rho})\right] = kT\,\frac{\pi d^3}{6}\,\eta\,\frac{(4-2\eta)}{(1-\eta)^3} \quad (13)$$

Equation (11) must be satisfied everywhere within the fluid, including the region far from the solid where $V = 0$ and $\rho = \widehat{\rho} = \rho_\infty$. Evaluation of equation (11) for this special case provides an expression for the ambient chemical potential,

$$\mu_\infty = kT\ln(\Lambda^3\rho_\infty) + \Delta\psi(\rho_\infty) + \rho_\infty(\Delta\psi' + \epsilon_{ff}C_{LJ}) \quad (14)$$

in which $C_{LJ} \approx -12\sigma^3$ is the integral of u, given by equation (4), over an infinite domain. Similarly, the pressure of the ambient gas follows directly from thermodynamic identities and the Maxwell relations applied to the Helmholtz free energy per unit mass, $a = f/\rho$.

$$p = \rho^2\left(\frac{\partial a}{\partial \rho}\right)_T = \rho kT\left(1 + \frac{d\psi}{d\eta}\right) + \frac{1}{2}\rho^2\epsilon_{ff}C_{LJ} \quad (15)$$

Thus for a given p and T, one can sequentially find ρ_∞ and μ_∞ from equations (15) and (14). The desired density distribution $\rho(\mathbf{r})$ is then obtained by solving equation (11), usually by numerical means.

Conventional Numerical Approach

Numerical solutions to equation (11) have been previously obtained using fine grids having spacing much smaller than the molecular diameter. This level of resolution is generally required to justify the assumption of uniform density within each grid zone. Under these circumstances the integral quantities U, $\Delta\psi$, and $\widehat{\Delta\psi'}$ in equation (11) can be replaced by summations over the grid using the distance between zone centers to evaluate the weight functions, ω and u. This discretization process yields a system of nonlinear algebraic equations that can be solved by iterative methods.

The prototypic adsorption problem is that of determining the density profile adjacent to a planar wall or within a planar slit or cylindrical pore. These geometries may be treated in a one-dimensional fashion since the density is expected to be relatively uniform in directions parallel to the pore walls.

The calculated variation of the normalized nitrogen density, $\rho^* = \rho\sigma^3$, with scaled distance, $x^* = x/\sigma$, from a graphite wall is illustrated in Figure 2 for a pressure slightly less than the bulk condensation pressure, p_0. Two solutions are shown. Although nearly identical near the adsorbent surface, they approach different asymptotes in the far field. In this region, one exhibits the density of a liquid, the other that of a gas. Since each solution represents a local minimum of Ω, we must select that one having the smaller free energy. For adsorption on a planar surface this is the gas-like solution at all pressures less than p_0.

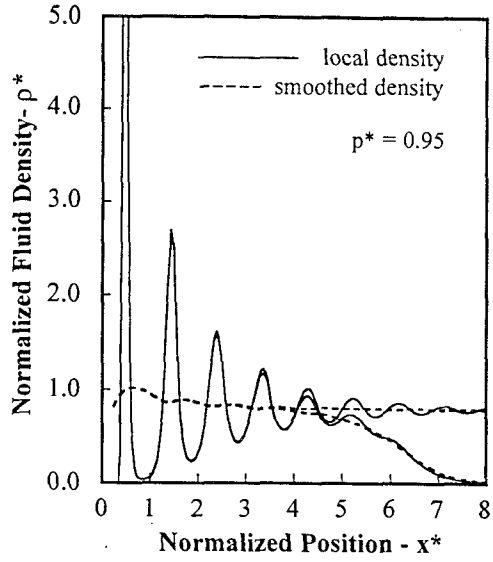

Figure 2. Density profiles adjacent to a solid surface. Gas-like and liquid-like solutions are indicated by solid lines. Corresponding smoothed densities, shown dotted, are used to calculate repulsions.

The oscillatory character of the local density profile is clearly apparent in the solid curves of Figure 2. The prominent peak adjacent to the pore wall is coincident with the minimum point of the wall potential, V. As such, it situated a distance roughly σ_{sf} from the center plane of the nearest atoms of the solid. Successive density peaks are separated by about one molecular diameter. This spacing maximizes the Lennard-Jones attraction while minimizing the hard sphere repulsion of adjacent peaks. With increasing distance from the wall, the width of the peaks increases and their amplitude decreases. Beyond a few molecular diameters, the density becomes nearly uniform over zones of molecular width.

The smoothed density, $\widehat{\rho}$, defined by equation (6) is also displayed in Figure 2 by the dashed curves. Despite extreme variations in the local density, $\widehat{\rho}$ varies smoothly between a maximum value of about unity near the pore wall to the ambient gas or liquid density in the far field. Moreover, the mean density cannot

greatly exceed unity anywhere since the corresponding repulsions calculated from equation (5) would then be excessive. For these two reasons, a mean density like $\widehat{\rho}$ is an attractive computational variable.

Conventional DFT solutions like those in Figure 2 entail substantial expenditures of computer time. Each density peak requires at least ten grid points to achieve an acceptable degree of definition. Further, since a minimal coverage of a few points per molecular diameter is always needed, if only to resolve the weighting functions themselves, there are typically 10 to 20 zones within one molecular diameter of any given point. All of these zones are close enough to contribute to the highly nonlinear repulsions. Because of this long-range nonlinear coupling, Tarazona recommended using weights of only 1/50 to update the unknown densities in his original iterative solution scheme [12]; larger weights generally lead to divergence. In an effort to decrease computing time we have employed adaptive gridding algorithms, banded relaxation schemes, and adaptive adjustment of iterative weights.

Despite all such efforts, more than 10^4 iterations are usually needed to converge a numerical solution like the one shown in Figure 2. The corresponding CPU time is several minutes on an SGI R8000 computer. Furthermore, generation of an adsorption isotherm typically requires 200 to 300 such solutions for a sequence of relative pressures p/p_0 ranging from 10^{-8} to unity. Finally, we must generally compute 50 to 100 such isotherms for different pore sizes if our goal is to determine pore size distributions from measured isotherms. Thus, a total of 10 to 30 thousand solutions are needed, each requiring 100 to 300 iterations when the most recent solution is used for initialization. Of course it is possible to store all of the results for future use, but they will only be applicable for a particular combination of pore geometry, adsorbent solid, adsorbate gas, and specimen temperature. Two-dimensional calculations addressing hysteresis in constricted and open-ended pores [18,19] require hours of computing to produce even one solution [19].

Locally Analytic Formulation

The objective of LADFT is to use our knowledge of the solution structure to reduce the computational effort. It is understood *a priori* that the first layer of adsorbed molecules will always be centered at the minimum of the external potential function V. It is also known that the separation between fluid molecules, and hence adsorbed layers, is very nearly the same as the shell diameter, $d \approx \sigma$, used in defining the hard sphere repulsion.

Thus, we begin by dividing the problem domain into calculational zones centered one molecular diameter apart. In one-dimensional problems, like those considered here, each of the slab-like zones represents a layer of adsorbed molecules. The zones nearest to the pore walls are first centered at the local minimum of the wall potential. From these locations, centers of subsequent zones are placed at integer multiples of the fluid molecular diameter. Any required nonuniformity of zone spacing due to non-integer pore widths is accommodated in a zone or pair of zones furthest from the pore walls.

Since essential features of LADFT are conveyed most easily through one-dimensional examples, the equations in the main text will hereafter be written using one-dimensional notation. These equations and solution procedures are generalized to their multidimensional form in Appendix A. However, nearly all of the ensuing discussion is applicable to both single and multidimensional problems.

Recognizing that fluid/solid interactions usually produce localized density peaks like those in Figure 2, we choose to represent the density profile within each zone by a function of the form

$$\rho(x) = \rho_i \, e^{-\alpha_i |x - x_i|^n} \tag{16}$$

in which ρ_i is the maximum density in the zone centered at x_i. The parameter α_i is the density profile coefficient that determines the shape of the profile in each zone. These shapes range from a singular spike for a large value of α_i to a uniform distribution when α_i is small. The exponent n may be taken as either unity, as done in the examples presented here, or two to obtain exponential or Gaussian peaks. This choice has negligible influence on the calculated mean density within zones, but affects instead only the less important magnitude of the peaks.

Because our primary aim is to calculate the total amount of adsorbed gas, we chose as our principal unknowns the average densities $\bar{\rho}_i$ within molecular-sized zones of volume v_i.

$$\bar{\rho}_i = \frac{\rho_i}{v_i} \int_{v_i} e^{-\alpha_i |x - x_i|^n} d\mathbf{r} \tag{17}$$

The integrals defining $\widehat{\rho}$ and U in equations (3) and (6) may then be written as summations over $\bar{\rho}_j$.

$$\widehat{\rho}(x_i) = \sum_j \omega_{ij} \bar{\rho}_j \quad \text{and} \quad U(x_i) = \sum_j u_{ij} \bar{\rho}_j \tag{18}$$

with the weights ω_{ij} and u_{ij} evaluated by integration over the jth zone

$$\omega_{ij}(x_i) = \frac{\rho_j}{\bar{\rho}_j} \int_{v_j} e^{-\alpha_j |x - x_j|^n} \omega(|\mathbf{r}_i - \mathbf{r}|) d\mathbf{r} \qquad (19)$$

where $\mathbf{r}_i$ refers to any fixed point on the center plane of the ith zone. The expression for $u_{ij}(x_i)$ is the same as equation (19) for $\omega_{ij}(x_i)$ except that ω is everywhere replaced by u.

The free energy functional may now be expressed in terms of volume integrals over the individual cells.

$$\Omega = \sum_i \int_{v_i} \rho(\mathbf{r}) \big[a(\mathbf{r}) + V(\mathbf{r}) - \mu_\infty \big] d\mathbf{r} \qquad (20)$$

This summation can be well approximated as

$$\Omega = \sum_i \bar{\rho}_i \big[\bar{a}_i + \bar{V}_i - \mu_\infty \big] v_i \qquad (21)$$

where

$$\bar{a}_i = kT \big[\ln(\Lambda^3 \bar{\rho}_i) - 1 \big] + \frac{1}{2} \bar{U}_i + \Delta\psi(\bar{\bar{\rho}}_i) \qquad (22)$$

The overbars appearing here indicate density weighted averages over the ith cell, as illustrated by the following definitions of $\bar{\bar{\rho}}_i$ and $\bar{U}$.

$$\bar{\bar{\rho}}_i = \frac{1}{\bar{\rho}_i v_i} \int_{v_i} \rho \, \widehat{\rho}_i d\mathbf{r} \quad \text{and} \quad \bar{U}_i = \frac{1}{\bar{\rho}_i v_i} \int_{v_i} \rho \, U \, d\mathbf{r} \qquad (23)$$

For computational purposes, these quantities may be rewritten in terms of the primary unknowns which are the mean densities in surrounding cells.

$$\bar{\bar{\rho}}_i = \sum_j \bar{\omega}_{ij} \bar{\rho}_j \quad \text{and} \quad \bar{U}_i = \sum_j \bar{u}_{ij} \bar{\rho}_j \qquad (24)$$

Here again, the overbars on the weights, $\bar{\omega}_{ij}$ and $\bar{u}_{ij}$, indicate that they have been averaged over the ith zone using the local density as a weight function.

$$\bar{\omega}_{ij}(x_i) = \frac{\rho_i}{\bar{\rho}_i v_i} \int_{v_i} e^{-\alpha_i |x - x_i|^n} \omega_{ij}(x) \, d\mathbf{r} \qquad (25)$$

As before, the analogous expression for $\bar{u}_{ij}(x_i)$ is obtained from equation (25) by replacing $\omega_{ij}(x_i)$ with $u_{ij}(x_i)$. We note that the quantities $\rho_i/\bar{\rho}_i$ appearing above, and hence all of the related weights, depend only on the grid geometry, on the pre-selected value of the exponent n, here taken as unity, and the profile coefficients α_i, as explained further in Appendix B.

The averaging process used in deriving equations (21) and (22) from equation (20) is mathematically exact for the linear terms involving $\bar{U}_i$ and μ_∞. The nonlinear $\Delta\psi$ term remains exact for a zone containing a singular spike ($\alpha \to \infty$) or in a region of uniform density ($\alpha \to 0$), but is otherwise approximate. The logarithmic term can be treated exactly for a locally exponential density profile like those used here, but the simpler approximation stated in equations (21) and (22) is adequate provided we adopt the following definition of the mean external potential.

$$\bar{V}_i = \ln \left[\frac{1}{v_i} \int_{v_i} e^{-V(\mathbf{r})} d\mathbf{r} \right] \qquad (26)$$

This ensures that the volume averaged equations will be exact in the low pressure limit where the logarithmic ideal gas term is in balance with the external attraction, $\bar{V}$.

A minimum of Ω now requires that its derivatives with respect to all $\bar{\rho}_i$ are identically zero, yielding a set of coupled algebraic equations of the form

$$kT \ln(\Lambda^3 \bar{\rho}_i) + \bar{U}_i + \bar{V}_i + \Delta\psi(\bar{\bar{\rho}}_i) + \widehat{\Delta\psi}' = \mu_\infty \qquad (27)$$

where

$$\widehat{\Delta\psi}' = \sum_j \Delta\psi'(\bar{\bar{\rho}}_j) \, \bar{\omega}_{ij} \, \bar{\rho}_j \qquad (28)$$

These are solved in sequence working outward from the pore walls. On each cycle, an improved estimate of each $\bar{\rho}_i$ is found by adjusting its value to satisfy the ith equation while holding the other $\bar{\rho}_j$ fixed. To perform this task we use a nonlinear equation solver called FZERO; comparable routines are available in most mathematical software libraries.

Most LADFT solutions converge within 5 to 20 iterations rather than the hundreds, or even thousands, of iterations required in the conventional approach. This rapid convergence is a direct benefit of averaging the equations over zones of molecular scale. When this is done, the mean density $\bar{\bar{\rho}}_i$ used in calculating the nonlinear repulsion terms is nearly the same as $\bar{\rho}_i$, the primary unknown in the ith equation. The resulting increase in diagonal dominance of the discretized equations eliminates any need for cautious weighting of the new $\bar{\rho}_i$ and greatly increases the convergence rate. This, together with a ten-fold reduction in the number of unknowns, reduces the required computing time by more than three orders of magnitude.

Density Profile Coefficients

The first steps in computing the mean density field using equations (27) and (28) are to determine appropriate values for the density profile coefficients,

α_i, and based on these values to calculate the corresponding weight coefficients, $\bar{u}_{ij}$ and $\bar{\omega}_{ij}$. As we will demonstrate, the weight coefficients (and therefore the total adsorbed gas) are relatively insensitive to the profile coefficients over a broad range of judicious approximations; because of this, we are afforded some measure of flexibility in our approach to determining these values. After briefly explaining the most rigorous approach, we then show that remarkably good results can be obtained using a set of fixed values for the profile coefficients. Appendix C describes a third, even simpler alternative that requires the least programming effort and yet yields results nearly as accurate as those presented here.

The most rigorous approach to determining the profile coefficients is to compute them directly from their definitions as a part of solving for the mean density field. In this case, the values of α_i are determined from an estimate of the mean density field using a discrete form of equation (16),

$$\alpha_{i\pm\frac{1}{2}} = \frac{1}{(|x_i - x_{i\pm\frac{1}{2}}|)^n} \ln\left[\frac{\rho(x_i)}{\rho(x_{i\pm\frac{1}{2}})}\right] \qquad (29)$$

where the subscripts $i \pm \frac{1}{2}$ refer to the edges of the ith zone. Similarly rewriting equation (27) in a discrete form, the logarithm of the density ratio can be replaced by the difference in potential between the same two points.

$$\ln\left[\frac{\rho(x_i)}{\rho(x_{i\pm\frac{1}{2}})}\right] = \frac{U + V + \Delta\psi(\widehat{\rho}) + \widehat{\Delta\psi'}}{kT}\Bigg|_i^{i\pm\frac{1}{2}} \qquad (30)$$

Evaluating the potentials at i and $i \pm \frac{1}{2}$ is straight forward but does entail weighted summations like those defined in equation (18). Although the values of α_i obtained from the right and left sides are not necessarily the same, the average of these two provides a good estimate for the mean value in a given zone. There is little need for greater precision since the weight functions vary weakly with the profile coefficients.

Combining equations (29) and (30) gives an explicit expression for the local profile coefficients in terms of the mean cell densities. Using this expression, new values of the profile and weight coefficients can be periodically computed from the current values of mean densities until convergence of both α_i and $\bar{\rho}_i$ is obtained.

From experience solving a broad range of sample problems, we have found that iterative adjustment of the profile coefficients is generally not required. Instead, a single set of these α's, may be held constant throughout all calculations. These physically-motivated values provide excellent results over all pore sizes and ambient pressures. In using these fixed profile coefficients, the corresponding weight coefficients need only be computed one time for a given geometry. Before presenting the preferred set of α's, it is instructive to first explore the consequences of alternative, even simpler, choices.

$\lvert i-j\rvert$	0	1	2	3
$\omega_{ij}(\infty)$	1	0	0	0
$\bar{\omega}_{ij}(\infty)$	1	0	0	0
$\omega_{ij}(0)$	0.82	0.09	0	0
$\bar{\omega}_{ij}(0)$	0.70	0.15	0	0
$u^*_{ij}(\infty)$	-3.77	-3.77	-0.39	-0.08
$\bar{u}^*_{ij}(\infty)$	-3.77	-3.77	-0.39	-0.08
$u^*_{ij}(0)$	-3.77	-3.09	-0.49	-0.09
$\bar{u}^*_{ij}(0)$	-3.77	-2.94	-0.63	-0.09

Table 1. Weight coefficients used to calculate attractions and repulsions between fluid masses in zones centered $|i-j|$ diameters apart. Self repulsions in the second column are much stronger than repulsions between neighboring zones. $u^*_{ij} = u_{ij}/\sigma^3$.

To illustrate the influence of the two simplest choices in assigning profile coefficients, we have computed the attractive weights coefficients, $\omega_{ij}(\alpha_i)$, and repulsive weight $u^*_{ij}(\alpha_i) = u_{ij}/\sigma^3$ coefficients for the limiting cases of $\alpha_i = \alpha = \infty$ and $\alpha_i = \alpha = 0$. These limiting values correspond to density profiles that are either all singular spikes or all uniform distributions, respectively. The results are presented in Table 1 for the exponent $n=1$. Integer values of $|i-j|$ across the top of the table indicate the distance between cell centers measured in molecular diameters. When $\alpha=\infty$, $\omega_{ii}=1$ and all other ω_{ij} are zero. In this limit of singular spikes in all zones, repulsive forces are localized within each zone, isolating the most severe nonlinearity of the equations. Even in zones of uniform density ($\alpha=0$), 70 to 80 percent of the repulsion resides locally in w_{ii}. This is in contrast to finely zoned calculations where nearly all of the repulsion arises from neighboring zones. The attractive weights shown in the lower part of the table are even less sensitive to the density profiles and so have still less impact on numerical stability and convergence.

To now illustrate the influence of these assumed density profiles on the mean density field and to-

tal adsorbed fluid, we have computed the adsorption isotherm for nitrogen on a flat graphite surface at a temperature of 77 K for three widely varying choices of the profile coefficients. In the first case, all profile coefficients are taken as $\alpha_i = \alpha = \infty$. In the second case, the coefficients are taken as $\alpha_i = \alpha = 0$. Again, these limiting values correspond to density spikes and uniform density distributions, respectively. In the third case, the assumed values of the profile coefficients are varied such that $\alpha_1 = \infty$, $\alpha_2 = 4/\sigma$, and $\alpha_i = 0$ for all $i \geq 3$. These values correspond to a density spike in the first zone adjacent to the surface, a roughly triangular profile in the second zone, and uniform density profiles in all zones further removed from the surface. The values of all other parameters used in these calculations are given later with the sample calculations for adsorption in pores.

The results of these comparative calculations of adsorption on a flat surface are shown in Figure 3. The ordinate in this figure, δ^*, is the amount of mass adsorbed per unit of wall area divided by the product of the molecular diameter, σ, and the bulk density of an unconfined saturated liquid, $\rho_\ell(p_0) \approx 0.8/\sigma^3$.

$$\delta^* = \frac{1}{\rho_\ell \sigma A} \int (\rho - \rho_\infty)\, d\mathbf{r} = \frac{1}{\sigma \rho_\ell} \sum (\bar{\rho}_i - \rho_\infty) \Delta x_i \quad (31)$$

This quantity may be loosely interpreted as the number of adsorbed layers. The abscissa in Figure 3 is the relative pressure, $p^* = p/p_0$, which is the absolute pressure normalized by the bulk saturation pressure for a temperature of 77 K.

The three solid curves in Figure 3 represent results for the three differing assumptions for the specified profile coefficients, indicated in the figure as all spikes, all uniform, and variable α. The isotherm depicted by a dashed curve and open circles was calculated using the smoothed density (SDA) formulation of DFT with a zone size of $\sigma/20$. For purposes of comparison, this latter result may be viewed as "exact".

Differences between the three LADFT solutions in Figure 3 result mainly from differences in the hard sphere repulsion. When the density is assumed uniform within each zone, the first layer of molecules has too little self repulsion, permitting $\bar{\rho}_1$ to reach excessive densities at low pressures. This behavior could have been anticipated from the entries in Table 1, since a narrowly peaked first layer should have a self repulsive weight of $\omega_{ii}(\infty) = 1.0$ rather than $\omega_{ii}(0) = 0.70$. However, as the pressure increases and more layers form, this approximation becomes more appropriate and the uniform density profiles give very good results. In the opposite extreme, in which the

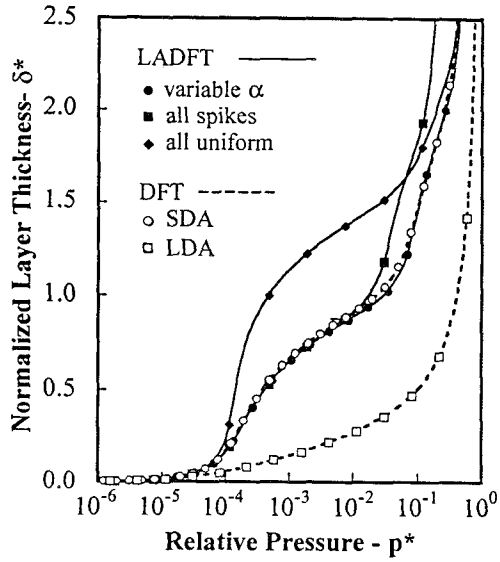

Figure 3. Calculated adsorption isotherm for a flat surface. LADFT solution with variable α (•) is nearly identical to the "exact" result (○) obtained by finely-zoned DFT with SDA repulsions.

density profiles are assumed to be spikes in all zones, the first layer fills correctly but the second forms too early because of too little repulsion and too much attraction between the first and second layers.

The LADFT solution in Figure 3 with variable α is clearly in excellent agreement with the fine-zoned DFT result. This composite of spike and uniform density profiles, with one transition zone between these extremes, permits proper formation of the first as well as all subsequent adsorbed layers. The results computed using this variable-α approximation with fixed profile coefficients are also nearly indistinguishable from those obtained using the most rigorous approach in which the profile coefficients are iteratively determined as a part of the solution.

Because the preassigned coefficients ($\alpha_1 = \infty$, $\alpha_2 = 4/\sigma$, and $\alpha_i = 0$ for $i > 2$) yield results quite comparable to the more rigorous iterative approach with much less programming and computational effort, these fixed α's will be used for all subsequent calculations.

One additional isotherm, not yet mentioned, has been included in Figure 3 to underscore the distinction between the present LA-DFT methodology and the local density approximation (LDA) sometimes used in conventional DFT. The LDA isotherm depicted by a dashed curve and open squares in Figure 3 was cal-

culated using conventional DFT numerical methods with a zone size of $\sigma/20$ assuming local equality of $\widehat{\rho}$ and ρ. In using ρ as a surrogate for $\widehat{\rho}$, the repulsion of a narrow peak is calculated as though it were surrounded, to a range of one diameter, by fluid having that same large density. The resulting excess repulsion suppresses the first and subsequent layers. In LADFT, by contrast, the repulsion of the first layer is much smaller because $\widehat{\rho}_1$ is equated to the mean density $\bar{\rho}_1$ (since $\bar{\omega}_{1,1} = 1$), which is several times smaller than the peak. As in all smoothed density approximations (SDA), the local repulsion in LADFT depends on the amount of mass within a range of one molecular diameter, rather than the local density. From these observations, it is clear that LDA-DFT and LADFT are not equivalent formulations of the problem.

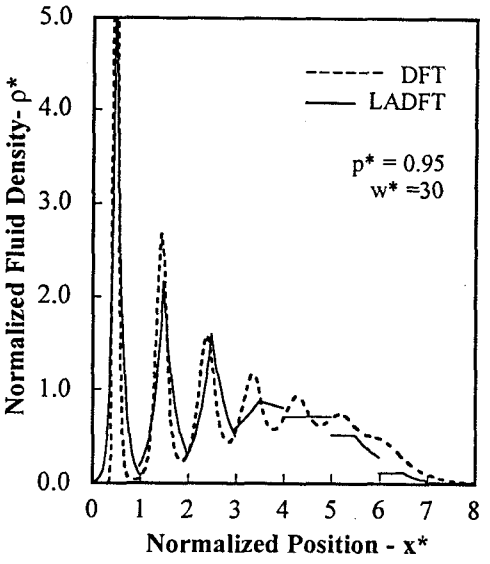

Figure 4. Comparison of density profiles for adsorption on a flat surface. LADFT reproduces first peaks quite well, but suppresses weaker oscillations. Peak spacing of DFT is slightly less than one diameter.

Reconstructing Density Profiles

Although a reconstruction the locally-analytic density profiles is not required in computing the amount of adsorbed fluid, such reconstruction provides insight into the nature of the solution and it serves as a valuable check on assigned values of the profile coefficients.

When the rigorous approach is used to iteratively adjust the density profile coefficients, their final values are already available for use in constructing density profiles. If, on the other hand, the α's are assigned and held fixed, the final profiles could be constructed using either the initial preassigned α's or, alternatively, those deduced from the calculated mean densities. If the initial α's were used, we would only reaffirm our expectation that the density profile of the first zone was supposed to be a spike, the second was transitional, and all others were uniform. For this reason, profile reconstruction is always based on the α's calculated from the converged mean densities using equations (29) and (30). As noted earlier, the values of α_i obtained by applying these equations to the right and left sides of a cell are averaged to obtain a single representative value of the profile coefficient.

The peak densities ρ_i at the zone centers may be determined from the calculated mean densities and profile coefficients by the following relationship that is derived by analytically integrating the presumed exponential density profile over a computational zone.

$$\rho_i(x_i) = \bar{\rho}(x_i)\frac{\alpha|x_i - x_{i+\frac{1}{2}}|}{[1 - \exp(-\alpha|x_i - x_{i+\frac{1}{2}}|)]} \qquad (32)$$

An analogous expression applies to Gaussian peaks. Finally, the density distributions within cells are constructed by direct substitution of ρ_i and selected values of $|x - x_i|$ into the exponential or Gaussian profiles defined by equation (16), this time maintaining the distinction between the α_i's that apply to the right and left sides.

To demonstrate the reconstruction process, we return to the previously discussed problem of nitrogen adsorption on a flat surface, focusing attention now on the density distribution for a relative pressure of $p^* = p/p_0 = 0.95$. In particular, we revisit the calculation in which the profile coefficients were assigned the fixed values of $\alpha_1 = \infty$, $\alpha_2 = 4/\sigma$, and $\alpha_i = 0$ for $i > 2$. The corresponding values of $\alpha^* = \alpha\sigma$ determined from the mean densities (after one iteration) using equations (29) and (30) are 12, 4.5, 2.9, and 0.5 for the first four layers. If we recalculate the density field using these new α's, none of the weight coefficients and none of the $\bar{\rho}_i$ changes by more than 3 percent, reinforcing our expectation that such iterations are usually unnecessary.

The piecewise continuous density profile, shown by a solid line in Figure 4 was constructed using the profile coefficients (12, 4.5, 2.9, 0.5) calculated after the first iteration of LADFT. This result is very similar to the fine-zoned DFT result, shown by a dashed curve. The first peaks reach maxima of 8.2 and 5.5 for the DFT and LADFT results, respectively. This 30 percent reduction in magnitude of first peak is comparable to the error incurred in a conventional DFT calculation run with a grid spacing of $\sigma/10$ instead

of the $\sigma/20$ spacing used to calculate the DFT result shown in Figure 4. These peak densities are sensitive not only to the grid spacing but also to details of the somewhat arbitrary choices made in modeling the hard sphere repulsion, either in DFT or in LADFT. Fortunately, the magnitude of the peak is not of critical importance to engineering applications. Overall, the character of the density profiles obtained by LADFT and DFT is remarkably similar and the amount of adsorbed fluid is nearly identical.

Exponential, rather than Gaussian functions, were used in constructing Figure 4 because these results are in better agreement with the finely zoned calculations. The corresponding Gaussian peaks are broader but smaller in amplitude. Regarding profile shapes, we also note that the second peak in Figure 4 has a nearly triangular shape and that this shape can be used, rather than an exponential function with $\alpha^* = 4/\sigma$, as a transition between zones having singular and uniform profiles.

The density peaks predicted by fine-zoned DFT are separated by slightly less than one molecular diameter, as apparent in Figure 4. In contrast, the LADFT peaks are, by assumption, coincident with zone centers that are separated by exactly one diameter. This unit spacing is appealing in its simplicity and produces isotherms that conform well with the more exact calculations. It would, of course, be possible to improve on this choice by simply using the observed DFT spacing or by determining with LADFT the spacing which minimizes the energy of an array of identical spikes. This would be the appropriate grid spacing for the highly oscillatory region, that being the only place where the spacing matters. However, since the spacing between layers actually depend on three-dimensional packing considerations, it may not be accurately predicted by one or two-dimensional models, whether implemented by LADFT or by DFT. Thus, it seems most appropriate to simply prescribe a layer spacing near unity or, alternatively, to use the basal plane spacing of a two or three-dimensional packing.

Sample Calculations for Slit Pores

The preceding LADFT calculations were restricted to adsorption on a flat external surface. To demonstrate the application to adsorption within pores, we now consider the adsorption of nitrogen at the normal saturation temperature of 77 K in slit pores of varying size. In each calculation the solid is graphite, having the potential of equations (8) and (9) with the parameters Δ, σ_s, ρ_s, and ϵ_{sf} taken as 3.35 Å, 3.48 Å, 0.11 Å^{-3}, and 0.78×10^{-14} ergs/molecule. The

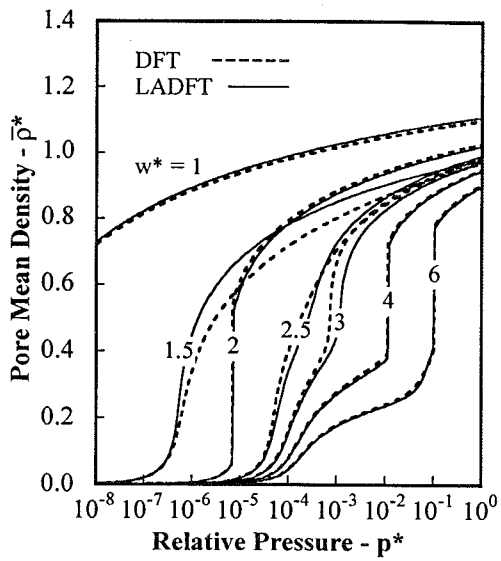

Figure 5. Adsorption isotherms for slits of width w^*. LADFT solutions agree very well with fine-zoned results, including occurrence and magnitude of condensation jumps in slits of width 2, 4, and 6.

mean diameter of the nitrogen molecule is $\sigma = 3.57$ Å, and the Lennard-Jones energy of approximately $\epsilon_{ff} \approx 1.86 \times 10^{-14}$ ergs/molecule is adjusted slightly, depending on C_{LJ} in equations (14) and (15), to ensure that the gas and liquid have equal energy when the pressure and temperature are the saturation values of 101 kPa and 77 K, respectively. The procedure used to adjust ϵ_{ff} is explained in Appendix C.

The normalized variables appearing in subsequent plots and discussion are based on length dimensions that are scaled by the adsorbate molecular diameter: $x^* = x/\sigma$, $w^* = w/\sigma$, $\delta^* = \delta/\sigma$, $u^*_{ij} = u_{ij}/\sigma^3$, $\alpha^* = \alpha\sigma$, $\rho^* = \rho\sigma^3$. Pressures are normalized by the bulk saturation pressure p_0, to obtain the dimensionless relative pressure $p^* = p/p_0$.

Adsorption isotherms for narrow pores bounded by planar walls are illustrated in Figure 5 for several choices of the normalized pore width, $w^* = w/\sigma$. The normalized pore mean density, $\bar{\rho}^* = \bar{\rho}\sigma^3$, is always gas-like at very low pressures, becoming liquid-like with increasing pressure. This transition occurs at lower pressures in smaller pores due to the increased overlap of attractive wall potentials. The isotherms of small pores ($w^* \leq 1.5$) are continuous, whereas discontinuous condensation jumps occur in large pores ($w^* \geq 4$). We further see that continuous solutions exist for pore sizes between 2 and 4, even though the solutions for $w^* = 2$ and $w^* = 4$ are both discontinuous. This rich-

ness of behavior has been explored previously by a number of investigators [5,6,9,10,13,14]. Our present purpose is simply to show that all of this complexity is captured by LADFT.

Adsorption isotherms like those in Figure 5 are constructed by first calculating the gas-like family of solutions starting from low pressure with initial densities set to the bulk gas density. After solving equation (27) for $\bar{\rho}_i$, the pore mean density, $\bar{\rho}(p)$, and free energy, $\Omega(p)$, are determined by integration over the pore. The pressure is then incremented, and the entire procedure is repeated using the last solution as the initial guess. A total of 300 solutions are calculated at even increments of $\log(p)$ before reaching the bulk condensation pressure, $p^* = 1$. The liquid-like solutions are then computed in a similar fashion, starting in this case from high pressure with all densities initialized at the bulk liquid density. For continuous isotherms both the liquid and gas families of solutions are identical. When they differ, the appropriate solution is the one having a smaller free energy, as computed using equation (21). The condensation jump then occurs at that pressure for which the two solutions have equal energies. This construction sequence is shared by DFT and LADFT; they differ only in the methodology used and time required to calculate density profiles for each pressure.

The agreement in Figure 5 between the LADFT and finely resolved DFT calculations is very good, particularly for pores having integer values of the normalized pore width. The result for $w^* = 1.5$ displays the largest disagreement that we have observed in comparing more than 100 isotherms for normalized pores sizes ranging from 0.8 to 40. Even this worst case is within acceptable bounds, and the inaccuracy associated with noninteger widths is no longer apparent for $w^* \geq 2.5$. The two sets of predictions are also remarkably consistent regarding the presence and magnitude of condensation jumps, in spite of the complexities noted earlier. Another feature consistent between LADFT and conventional DFT is the crossing of isotherms for small pore sizes; this is a consequence of steric effects better illustrated by the next figure.

The pore mean density at a relative pressure of unity is plotted in Figure 6 as a function of the normalized pore width. The density peaks are associated with pores that ideally accommodate an integer number of adsorbate layers. The peaks are not quite coincident with integer pore widths because the minimum of the wall potential is situated at $x^*_{\mathrm{vmin}}/\sigma \approx 0.473$, rather than 0.5, and because the preferred spacing between peaks is somewhat less that σ. Pores smaller than $w^* \approx 0.7$ are too small to admit even one gas molecule, while very wide pores have a mean density

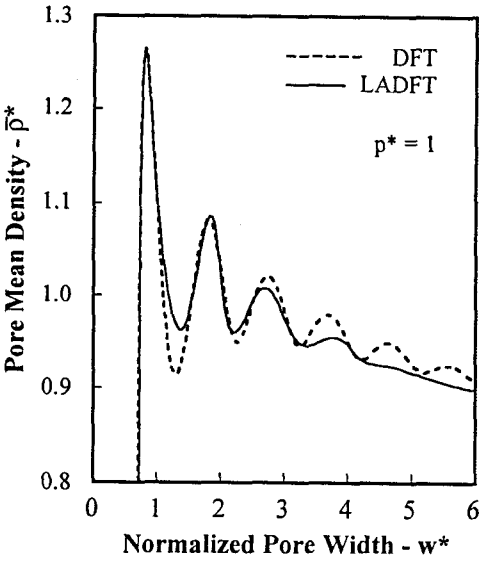

Figure 6. Variation of pore mean density of a saturated liquid with pore width. Steric effects are predicted within a few percent by LADFT, indicating that noninteger pore widths are not problematic.

approaching that of the unconfined saturated liquid, $\rho^*_l(p_0) \approx 0.8$.

The comparison in Figure 6 shows that LADFT performs very well despite the introduction of zones having irregular width at the pore center. The number of zones, N is determined by rounding $w^* - 2x^*_{\mathrm{vmin}} + 1 \approx w^*$ to the next larger integer. When N is odd, the middle zone is always centered at $x^* = w^*/2$. For all $N > 1$, centers of the first zones are placed at the minima of the wall potential; successive centers are then positioned σ apart until the next one would cross the center plane. Thus, when the pore width is slightly greater than $2x^*_{\mathrm{vmin}} \approx 1$, the center zone is split in half. The resulting half zones grow with increasing w^* until passing $w^* \approx 2$ at which point a third, very narrow, zone is introduced in the center. It grows to unity, then splits in two, and the process repeats. This gridding procedure avoids the incidental discontinuities that would otherwise accompany changes in the number of zones.

Table 2 shows a comparison between CPU times required to construct single 300-point adsorption isotherms like those in Figure 5. All calculations were performed on an SGI R8000 computer operating at 75 MHz. Initial values for each new pressure were taken from the preceding solution. Iterations were continued until the relative change in density on a

w^*	DFT	LADFT	Ratio
2	665	0.91	730
4	1389	1.37	1013
8	3366	1.46	2305
16	10793	2.53	4266
32	37429	5.90	6343

Table 2. CPU time (seconds) required to construct single adsorption isotherms by DFT and by LADFT. The ratio of these two times, shown in the far right column, increases with increasing pore width.

single cycle was less than 10^{-6} at every point. In the interest of fairness, we used a relatively course grid size of $\sigma/10$ for the conventional DFT calculations. This grid spacing provides only a three-point resolution of the first peak and shaves its amplitude by 30 percent, as noted earlier. Even so, the ratios of the CPU times for DFT and LADFT ranged from 730 to 6343 for pores sizes ranging from 2 to 32 molecular diameters. If we had used a grid spacing of $\sigma/20$ for DFT, as needed to obtain the better resolved profiles in Figure 2, these ratios would have increased by factors of 2 to 4 depending on the size of the domain.

These reductions in CPU time of 10^3 to 10^4 are due in part to the 10-fold difference in the number, M, of grid lines per molecular diameter. This should account for a factor of 100 in the number of operations required per iteration since the summations at Mw^* grid points each involve contributions from $Mr^*_{\max}$ neighbors, where $r^*_{\max}$ is the normalized cutoff range of the Lennard-Jones potential, taken as 3.5 in our calculations. The remaining factor of 10 to 100 comes from reducing the required number of iterations by localizing repulsive nonlinearities within cells. These same considerations are expected to reduce CPU times by roughly 10^6 in two-dimensional applications.

Summary

Density functional theory (DFT) is widely used to determine fluid density distributions in microporous materials. In the DFT methodology, minimizing the Helmholtz free energy functional leads to a system of equations relating the local chemical potential to the van der Waals attractions and hard sphere repulsions of surrounding material. To solve these equations by traditional numerical methods requires a very substantial computing effort since the discretization grid must be fine enough to resolve density peaks much narrower than molecular dimensions.

In this present work, we avoid numerical resolution of sub-molecular scales by averaging the governing equations over zones of molecular size using analytical profiles to describe the spatial density variation within each zone. We find that these local density variations are well represented by exponential functions, which may vary from uniform distributions to singular density spikes as the exponential profile coefficient varies from small to large values. The profile coefficients thus represent the reciprocal of the characteristic width of the density profile within a given cell.

Substituting these locally-analytic profiles into the governing equations and integrating over each computational cell yields a system of coupled equations for the mean cell densities and corresponding profile coefficients. The profile coefficients, which play a secondary role in these equations, may be determined iteratively as part of solving the fully coupled system of equations, or alternatively may be preassigned and held fixed. Generally, convergence of the profile coefficients is sufficiently fast that preassigned values, if properly selected, provide very good results.

Adsorption isotherms and condensation pressures calculated using this locally-analytic density functional theory (LADFT) are in excellent agreement with those predicted using the traditional implementation of DFT. Agreement between LADFT and traditional DFT predictions of the mean pore density is generally within a few percent for pressures spanning ten orders of magnitude and for pore sizes ranging from one molecular diameter up to the continuum limit. This level of agreement is obtained using preselected values of the profile coefficients corresponding to a singular density spike adjacent to any pore wall, one neighboring transition profile having a nearly triangular shape, and a series of uniform density zones still further removed from the pore wall.

The main benefit of the integral LADFT approach is to reduce computing times by a factor ranging from 10^3 to 10^4. Such dramatic improvements should permit broader application of density functional theory. For example, determining pore size distributions from measured adsorption isotherms using traditional DFT normally requires several days to compute the required family of single-pore isotherms for wide range of pore sizes. These can now be computed in about one minute. Two-dimensional calculations, which formerly entailed several hours of com-

puting to produce one solution for a single pressure and single pore size, can now be completed in a few seconds.

One long-range goal of this modeling effort is to incorporate molecular-scale physics into engineering-scale analyses of adsorption and transport in an assemblage of interconnected pores of varying sizes. The integral formulation of DFT presented here brings us a step closer to that goal by eliminating the need for numerical resolution of sub-molecular scales.

Nomenclature

a	Helmholtz free energy per unit mass
d	molecular diameter used to calculate repulsions
f	Helmholtz free energy per unit volume
k	Boltzman's constant
M	number of zones per molecular diameter
p	pressure
$\mathbf{r}$	position vector
T	temperature
u	Lennard-Jones pair potential
U	fluid-fluid attraction
V	external potential induced by solid walls
v	volume of a computational cell
w	pore width
x	distance from solid surface
z	distance from center plane of wall molecules
α	exponential decay constant
δ	thickness of adsorbed film
Δ	basal plane spacing of wall molecules
$\Delta\psi$	excess hard sphere repulsion
ϵ	well depth of Lennard-Jones potential
η	volume fraction occupied by molecules
Λ	de Broglie wave length
μ	chemical potential
ρ	fluid density
σ	molecular diameter
ω	weight function defining smoothed density
Ω	grand potential energy functional

Subscripts

ff	fluid-fluid
sf	solid-fluid
ij	indices of computational grid
ℓ	bulk liquid
max	cutoff range of Lennard-Jones potential
0	condensation point of bulk fluid
vmin	location where wall potential, V, is minimum

Superscripts

$'$	derivative or integration variable
$*$	normalized quantity (length scaled by σ)
$\bar{}$	density weighted average over a grid zone
$\hat{}$	weighted average used to calculate repulsion

Acknowledgment

This work was sponsored by the Engineered Materials and Processes Research Foundation at Sandia National Laboratories.

References

1. D. M. Ruthven, *Principles of Adsorption and Adsorption Processes*, Wiley-Interscience, NY, 1984.

2. S. J. Gregg and K. S. W. Sing, *Adsorption, Surface Area, and Porosity*, Academic Press, London, 1983.

3. M. M. Dubinin, "Fundamentals of the Theory of Adsorption in Micropores of Carbon Adsorbents: Characteristics of Adsorption Properties and Microporous Structures", *Carbon*, Vol. 27, No. 3, 457-467, 1989.

4. N. A. Seaton, J. P. R. B. Walton, and N. Quirke, "A New Analysis Method for the Determination of the Pore Size Distribution of Porous Carbons from Nitrogen Adsorption Measurements", *Carbon*, Vol. 27, No. 6, 853-861, 1989.

5. C. Lastoskie, K. E. Gubbins, and N. Quirke, "Pore Size Distribution Analysis of Microporous Carbons: A Density Functional Theory Approach", *J. Phys. Chem.*, Vol. 97, No. 18, 4786-4796, 1993.

6. J. P. Olivier, W. B. Conklin, and M. V. Szombathely, "Determination of Pore Size Distributions from Density Functional Theory: A Comparison of Nitrogen and Argon Results", *Characterization of Porous Solids III*, edited by J. Rouquerol, F. Rodriguez-Reinoso, K. S. W. Sing, and K. K. Unger, Studies in Surface Science and Catalysis, Vol. 87, 81-89, Elsevier Science, 1994.

7. S. Brunauer, L. E. Copeland, and D. L. Kantro, *The Langmuir and BET Theories*, The Solid-Gas Interface, edited by E. A. Flood, Marcel Dekker NY, 1967.

8. G. Horvath and K. Kawazoe, "Method for the Calibration of Effective Pore Size Distribution in Molecular Sieve Carbon", *J. Chem. Eng. Japan*, Vol. 16, No. 6, 470-475, 1983.

9. B. K. Peterson, K. E. Gubbins, G. S. Heffelfinger, U. Marini, B. Marconi, and F. van Swol, "Lennard-Jones Fluids in Cylindrical Pores: Nonlocal Theory and Computer Simulation", *J. Chem Phys.*, Vol. 88, No. 10, 6487-6500, 1988.

10. J. P. R. B. Walton and N. Quirke, "Capillary Condensation: A Molecular Simulation Study", *Molecular Simulation*, Vol. , 361-391, 1989.

11. D. E. Sullivan and M. M. Telo de Gama, *Wetting Transitions and Multilayer Adsorption at Fluid Interfaces*, Fluid Interfacial Phenomena, edited by C. A. Croxton, John Wiley, NY, 1986.

12. P. Tarazona, "Free-energy Functional for Hard Spheres", *Phys. Rev. A, Vol. 31*, No. 4, 2672-2679, 1985.

13. C. Lastoskie, K. E. Gubbins, and N. Quirke, "Pore Size Heterogeneity and the Carbon Slit Pore: A Density Functional Theory Model", *Langmuir*, Vol. 9, 2693-2702, 1993.

14. A. Papadopoulou, F. van Swol, U. Marini, and B. Marconi, "Pore-end Effects on Adsorption Hysteresis in Cylindrical and Slitlike Pores", *J. Chem. Phys.*, Vol. 97, No. 9, 6942-6952, 1992.

15. J. P. Olivier and W. B. Conklin, "Determination of Pore Size Distributions from Density Functional Theoretic Models of Adsorption and Condensation within Porous Solids", in DFT Software, available from Micromeritics Instrument Corporation, Norcross, GA, 30093, USA.

16. J. N. Israelachvivi, *Intermolecular and Surface Forces*, Academic Press, San Diego, 1994.

17. W. A. Steele, *The Interaction of Gases with Solid Surfaces*, Pergamon Press, Glasgow, 1974.

18. C. Lastoskie, K. E. Gubbins, and N. Quirke "Pore Size Distribution Analysis and Networking: Studies of Microporous Sorbents", *Characterization of Porous Solids III*, edited by J. Rouquerol, F. Rodriguez-Reinoso, K. S. W. Sing, and K. K. Unger, Studies in Surface Science and Catalysis, Vol. 87, 51-60, Elsevier Science, 1994.

19. S. Sokolowski and J. Fischer, "Liquid-Vapour Density Profiles for Fluids in Pores from Density Functional Theory", *J. Chem. Soc. Faraday Trans.*, Vol. 89, No. 5, 789-794, 1993.

Appendix A: Multidimensional Formulation

The purpose of this appendix is to briefly outline the application of locally analytic DFT to two and three-dimensional geometries. The region of interest is first subdivided into zones with centers spaced one molecular diameter apart in directions of density variation. As in any numerical analysis, there is no need to subdivide the domain in directions of uniform density.

The gridding procedure for multidimensional applications is essentially the same as in one dimension. The first layers of zones should still conform to adsorptive solid boundaries. However, by now laterally subdividing the first and subsequent layers into zones of molecular size, allowance is made for density variations within layers. Irregular geometries pose no fundamental obstacles, since it is only necessary to divide the two or three dimensional space of interest into zones centered roughly one molecular diameter apart, placing odd sized zones in regions furthest from boundaries.

The fluid density within a three-dimensional cell centered at $\mathbf{r}_i$ may generally vary with all three position coordinates, as in the following extension of equation (16)

$$\rho(\mathbf{r}) = \rho_i \, f(\mathbf{r}, \mathbf{r}_i) \tag{A1}$$

where $\mathbf{r} = (x, y, z)$, $\mathbf{r}_i = (x_i, y_i, z_i)$, and

$$f(\mathbf{r}, \mathbf{r}_i) = e^{-\alpha_i |x - x_i|^n - \beta_i |y - y_i|^n - \gamma_i |z - z_i|^n} \tag{A2}$$

The three exponential decay constants appearing here may then be calculated from cross-cell potential variations in the three orthogonal directions using equations analogous to (29) and (30). If there is no potential gradient in one of these directions, the corresponding coefficients will be zero and the solution will revert to that for a lower dimensionality.

The mean cell density defined earlier by equation (17) is, in general, given by

$$\bar{\rho}_i = \frac{\rho_i}{v_i} \int_{v_i} f(\mathbf{r}, \mathbf{r}_i) \, d\mathbf{r} \tag{A3}$$

and the weights ω_{ij} of equation (19) are evaluated by integration over the jth cell.

$$\omega_{ij}(\mathbf{r}_i) = \frac{\rho_j}{\bar{\rho}_j} \int_{v_j} f(\mathbf{r}, \mathbf{r}_i) \, \omega(|\mathbf{r}_i - \mathbf{r}|) \, d\mathbf{r} \tag{A4}$$

These repulsion weights are then averaged over the ith cell to obtain

$$\bar{\omega}_{ij}(\mathbf{r}_i) = \frac{\rho_i}{\bar{\rho}_i v_i} \int_{v_i} f(\mathbf{r}, \mathbf{r}_i) \, \omega_{ij}(\mathbf{r}) \, d\mathbf{r} \tag{A5}$$

To calculate the corresponding attractive weight coefficients, $u_{ij}(\mathbf{r}_i)$ and $\bar{u}_{ij}(\mathbf{r}_i)$, it is only necessary to replace $\omega(|\mathbf{r}_i - \mathbf{r}|)$ and $\omega_{ij}(\mathbf{r})$ in equations (A4) and (A5) with $u(|\mathbf{r}_i - \mathbf{r}|)$ and $u_{ij}(\mathbf{r})$, respectively. Although we have used catresian coordinates to describe three-dimensional density variations within cells, the cell centers need not be located at the intersections of a rectangular grid. They could just as well be chosen to conform with a three-dimensional packing of spheres or, alternatively, the interstices of a porous adsorbent or a zeolite.

Because the governing equations involve integral rather than differential operators, the numerical solution scheme is nearly insensitive to the chosen grid geometry. Indeed, the summations used to define Ω, $\bar{U}$, and $\bar{\widetilde{\rho}}$ in equations (20) through (24) are applicable to all geometries in any number of dimensions. The only differences arise in the required number of zones, the directions over which the summations extend, and the evaluation of weight coefficients.

Appendix B: Calculation of Integral Weights

The weight coefficients defined by equations (A4) and (A5) can always be evaluated by direct numerical integration over all three space dimensions. However, it is usually more efficient to perform some or all of these integrations analytically. Both alternatives are explained below.

To evaluate the weight coefficients by direct numerical integration, each of the molecular-scale calculational cells must be subdivided into intervals small enough to resolve variations in both the local density profile, $f(\mathbf{r},\mathbf{r}_i)$, and the weight functions, $\omega(\mathbf{r})$ or $u(\mathbf{r})$, themselves. Since these integrations are usually performed only once, the required CPU time is a small fraction of the total time spent in solving the equations. Thus, there is no significant penalty in using 20 to 40 integration zones per molecular diameter. In a two or three-dimensional problem the differential volume element, $d\mathbf{r}$, is expanded as the product of dx, dy, and dz; numerical integrations are then performed over all three directions. It is, however, possible to integrate analytically over any direction in which the density is uniform, as illustrated below for one-dimensional geometries.

When the density variation is one-dimensional, as in the examples presented in the main text, numerical integrations need only extend over that one dimension. For example, if the density varies with x alone, equation (A4) may be written as

$$\omega_{ij}(x_i)=\frac{\rho_j}{\bar{\rho}_j}\int_{x_{j-\frac{1}{2}}}^{x_{j+\frac{1}{2}}} e^{-\alpha_j|x-x_j|^n}\int_0^\infty \omega(r)2\pi\zeta\, d\zeta\, dx \quad \text{(A6)}$$

Here, $r=|\mathbf{r}|$ is the distance between a fixed reference point (x_i,y_i,z_i) in the ith slab and a moving integration point (x,y,z) in the jth slab. That distance is composed of a ξ-component, $\xi=|x-x_i|$, parallel to the x axis and a ζ-component that lies in the perpendicular (y,z) plane.

$$r=\sqrt{(\xi^2+\zeta^2)} \quad \text{(A7)}$$

$$\zeta=\sqrt{(y-y_i)^2+(z-z_i)^2} \quad \text{(A8)}$$

With these definitions, the integration over ζ can be performed analytically for any given choice of the weight functions $\omega(r)$ and $u(r)$. Using the particular functions defined by equations (4) and (7), respectively,

$$\begin{aligned}\int_0^\infty \omega(r)2\pi\zeta\, d\zeta &= \frac{1}{\sigma}(1-3\xi^{*2}+2\xi^{*3}) && \xi\le 1\\ &= 0 && \xi>1\end{aligned} \quad \text{(A9)}$$

and

$$\begin{aligned}\int_0^\infty u(r)2\pi\zeta\, d\zeta &= -4\pi\sigma^2\left(\frac{1}{2}-\frac{1}{5}\right) && \xi\le 1\\ &= -4\pi\sigma^2\left(\frac{\xi^{*-4}}{2}-\frac{\xi^{*-10}}{5}\right) && \xi>1\end{aligned} \quad \text{(A10)}$$

in which $\xi^*=\xi/\sigma$. These results are then substituted into equations (A6) and ultimately into (A5) before integrating over the x, or equivalently ξ, direction. Those integrals depend upon the shapes of the density profiles in the jth and ith zones, respectively, and must usually be evaluated numerically for particular values of α_j and α_i.

The ratio of the maximum to the mean cell density, $\rho_i/\bar{\rho}_i$, appearing in equations (A4), (A5), and (A6) can generally be determined by analytical integration of the presumed density profile over the ith zone. The defining equation for this process is (A3), and the result is given, for $n=1$ and for any finite α, by equation (32) of the main text.

In the degenerate case of a singular density profile, the process of density weighted integration over a cell is replaced by simply forming the product of the cell mass, $\bar{\rho}_i v_i$, with the value of the integrand that applies at the cell center. By this reasoning, the weight coefficients, $\omega_{i,j}$ and $u_{i,j}$ defined by equation (A6), can be obtained for singular cells by simply evaluating the right hand sides of equations (A9) and (A10) for $\xi=|x_i-x_j|$ and multiplying the result by $\Delta x_j=|x_{j+\frac{1}{2}}-x_{j+\frac{1}{2}}|$. The $\bar{\rho}_j$ appearing in the cell mass cancels with the $\bar{\rho}_j$ in the denomonator of equation (A6), such that the weights are independent of $\bar{\rho}_j$. Although the weights are always independent of $\bar{\rho}_i$ and $\bar{\rho}_j$, they do depend upon α_i and α_j.

Based on our experience with alternative formulations of LADFT, we can recommend all three of approaches enumerated below, varying from the simplest to the most general.

(1) To obtain good results for the least effort, use singular density profiles ($\alpha_i=\infty$) in all zones, particularly if the problem is multidimensional. This approach is further detailed in Appendix C where sample results are also included.

(2) A good balance between simplicity and accuracy is afforded by using the preselected values of profile coefficients that are applied in the sample calculations of the main text, $\alpha_1 = \infty$, $\alpha_2 = 4/\sigma$, and $\alpha_i = 0$ for $i \geq 3$.

(3) To obtain maximum generality, the profile coefficients may be determined as a part of the solution. After converging the mean cell densities for some initial choice of the α's, equations (29) and (30) are used to determine new values of the α's. The weight coefficients must then be recalculated for any zones that experience significant changes in α. Although such iterations could become quite time consuming, the weight coefficients are relatively weak functions of the profile coefficients, and the initial guesses suggested in method (2) above are sufficiently accurate for all of the problems we have solved. For these reasons, the recalculation of α's serves mainly as a consistency check.

Appendix C: Minimizing Programming Effort

Very good results can be achieved with a minimal computer programming effort by simply assuming that all of the mass within any cell is located at the cell center. Under this approximation, identified with profile coefficients that are all infinite, the entire density distribution is described by an array of singular spikes (actually singular sheets in one dimension) separated from one another by one molecular diameter.

The advantage of this approach is that the weight coefficients depend only on the distance between zone centers, so the only integrations required are those extending over directions in which the density is uniform. These integrals have already been evaluated in equations (A9) and (A10) for the geometry requiring the greatest amount of prior analysis, that is, for the one-dimensional case. Two-dimensional geometries require analytic integration over one Cartesian dimension; three-dimensional problems require none at all.

Adsorption isotherms calculated by this method for slit pores are shown in Figure A1. As in the analogous Figure 5, results obtained by LADFT, this time with all α_i set to ∞, are compared with "exact" isotherms computed by conventional finely zoned DFT. It is seen that the condensation jumps and high-pressure portions of the isotherms are quite well predicted by LADFT but that a relatively moderate error is committed in the low pressure region when the first layers are forming. These observations appear to conflict with earlier comparisons in Figure 3 of isotherms for a flat external surface; there, the isotherm for $\alpha_i = \alpha = \infty$ was correct at low pressure but deviated at high pressure. The explanation for this apparent inconsistency lies in the fact that all of the isotherms in Figure 3 used the same value of the Lennard-Jones energy, ϵ_{ff}, whereas Fig. A1 was constructed using a slightly different value of ϵ_{ff} that produces bulk condensation (for this model with $\alpha_i = \alpha = \infty$) at the correct pressure.

Recall that any DFT analysis, conventional or locally-analytic, is begun by determining the Lennard-Jones energy, ϵ_{ff}, consistent with the model in use. This is done using a nonlinear equation solver, FZERO in our work, to iteratively adjust the value of ϵ_{ff} so that the energy of the bulk liquid and the bulk gas are identical at the known bulk condensation pressure, p_0, corresponding to the isotherm temperature. To this end, a nested root-finding operation is performed, with the outer loop adjusting the value of ϵ_{ff} and the inner loops adjusting the values of the bulk liquid and bulk vapor densities, ρ_l and ρ_g, to find the two roots of equation (14) for a candidate ϵ_{ff}. For those two densities, the corresponding energies, Ω_l and Ω_g are calculated from a simplified version of equation (1), analogous to equation (14), that applies to a bulk fluid in the absence of an external potential. Although two density roots and the corresponding energies can be found for a broad range of ϵ_{ff}, there is only one value of ϵ_{ff} for which these energies are identical.

The Lennard-Jones energy ϵ_{ff}, so determined, depends upon the modeling assumptions through the numerical value of C_{LJ} appearing in equations (14), (15), and (A14). C_{LJ} is the density weighted integral of the Lennard-Jones pair potential, u, over an infinite domain containing, for $\alpha_i = \infty$, an infinite array of density spikes or sheets. This configuration is not identical to the customary case of a bulk fluid having a spacially uniform density corresponding to $\alpha_i = 0$. It is noted that in the general case of variable α the properties of the bulk fluid should be based upon $\alpha_i = 0$, because that is the physical state preferred by that model in the absence of, or remote from, solid boundaries.

The numerical values of $C^*_{\text{LJ}} = C_{\text{LJ}}/\sigma^3$ for $\alpha_i = 0$ and $\alpha_i = \infty$ are approximately -11.09 and -12.25, as obtained by horizontal summation of the entries in Table 1, taking into account that all but the first entry, for $\bar{u}_{ii}$, must be counted twice because those layers are present on both sides of any central slab of fluid. It follows, further, that a larger magnitude of C_{LJ} results in a smaller value of ϵ_{ff}, since the product $\epsilon_{ff} C_{\text{LJ}}$ must be nearly the same for all configurations having the same bulk condensation pressure.

This 10 percent reduction in the Lennard-Jones energy of the singular-spike model reduces the self

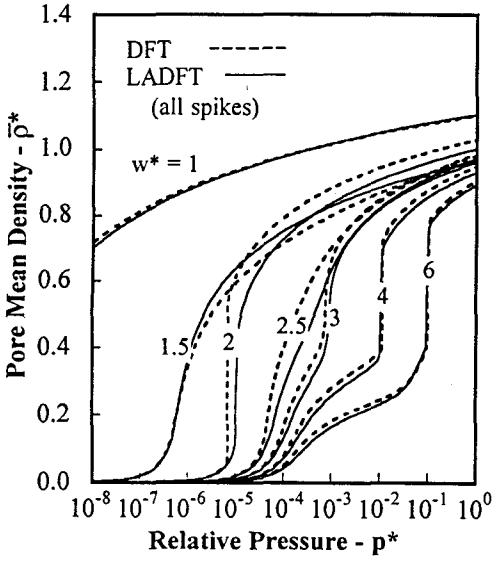

Figure A1. Adsorption isotherms predicted by LADFT are in good agreement with "exact" DFT results even when the density profiles are presumed singular in all zones. Although agreement is slightly degraded from that shown earlier in Figure 5, required computer coding is simplified.

attraction of the first layer and, hence, reduces the amount of adsorption occurring at low pressure. However, with increasing pressure the growth of a thickening layer and the occurrence of pore condensation depend on the collective attraction of multiple fluid layers. This bulk attraction must necessarily be quite similar for all models that use the preceding methodology to determine ϵ_{ff}. Overall, the mathematical accuracy of even the simplest singular-spike version of LADFT should be more than adequate for most purposes.

UNLIMITED RELEASE
INITIAL DISTRIBUTION

0513 R. J. Eagan, 1000
1435 H. J. Saxton, 1800
1434 G. E. Pike, 1802
0367 P. A. Cahill, 1812
1407 C. L. Renschler, 1812
1407 J. H. Aubert, 1815
1407 R. R. Lagasse, 1815
1349 C. J. Brinker, 1815
0710 G. A. Carlson, 6211
9001 T. O. Hunter, 8000
Attn: M. E. John, 8100
R. C. Wayne, 8400
D. L. Crawford, 8900
9420 L. A. West, 8200
9405 J. M. Hruby, 8230
9405 R. W. Crocker, 8230
9405 L. L. Whinnery, 8230
9054 W. J. McLean, 8300
Attn: C. W. Robinson, 8301
L. A. Rahn, 8351
F. P. Tully, 8353
D. R. Hardesty, 8361
R. W. Carling, 8362
9163 W. Bauer, 8302
9042 R. J. Kee, 8303
9042 G. H. Evans, 8345
9042 J. F. Grcar, 8345
9042 S. K. Griffiths, 8345 (10)
9042 C. M. Hartwig, 8345
9042 R. S. Larson, 8345
9042 R. H. Nilson, 8345 (10)
9405 T. M. Dyer, 8700
9904 W. D. Wilson, 8700
9403 M. I. Baskes, 8712
9161 W. G. Wolfer, 8717
9403 W. R. Even, 8713
9403 T. J. Shepodd, 8713
9403 J. C. F. Wang, 8713
0828 R. D. Skocypec, 9102
0834 A. C. Ratzel, 9112
0834 M. J. Martinez, 9112
0834 W. L. Hermina, 9111
0826 M. R. Baer, 9112
1111 L. J. Frink, 9225
1111 F. B. Van Swol, 9225
9021 Technical Communications, 8535
for OSTI (10)
9021 Technical Communications, 8535
8099 Technical Library, 13414 (4)
9018 Central Technical Files, 8523-2 (3)